A magnetic resonance spectroscopy driven initialization scheme for active shape model based prostate segmentation

Robert Toth[a], **Pallavi Tiwari**[a], **Mark Rosen**[b], **Galen Reed**[c], **John Kurhanewicz**[c], **Arjun Kalyanpur**[d], **Sona Pungavkar**[e], and **Anant Madabhushi**[a,*]

[a] Rutgers, The State University of New Jersey, Department of Biomedical Engineering, Piscataway, NJ 08854, USA

[b] University of Pennsylvania, Department of Radiology, Philadelphia, PA 19104, USA

[c] *University of California, San Francisco, CA, USA*

[d] *Teleradiology Solutions, Bangalore 560 048, India*

[e] Dr. Balabhai Nanavati Hospital, Mumbai 400 056, India

Abstract

Segmentation of the prostate boundary on clinical images is useful in a large number of applications including calculation of prostate volume pre- and post-treatment, to detect extra-capsular spread, and for creating patient-specific anatomical models. Manual segmentation of the prostate boundary is, however, time consuming and subject to inter- and intra-reader variability. T2-weighted (T2-w) magnetic resonance (MR) structural imaging (MRI) and MR spectroscopy (MRS) have recently emerged as promising modalities for detection of prostate cancer *in vivo*. MRS data consists of spectral signals measuring relative metabolic concentrations, and the metavoxels near the prostate have distinct spectral signals from metavoxels outside the prostate. Active Shape Models (ASM's) have become very popular segmentation methods for biomedical imagery. However, ASMs require careful initialization and are extremely sensitive to model initialization. The primary contribution of this paper is a scheme to automatically initialize an ASM for prostate segmentation on endorectal *in vivo* multi-protocol MRI via automated identification of MR spectra that lie within the prostate. A replicated clustering scheme is employed to distinguish prostatic from extra-prostatic MR spectra in the midgland. The spatial locations of the prostate spectra so identified are used as the initial ROI for a 2D ASM. The midgland initializations are used to define a ROI that is then scaled in 3D to cover the base and apex of the prostate. A multi-feature ASM employing statistical texture features is then used to drive the edge detection instead of just image intensity information alone. Quantitative comparison with another recent ASM initialization method by Cosio showed that our scheme resulted in a superior average segmentation performance on a total of 388 2D MRI sections obtained from 32 3D endorectal *in vivo* patient studies. Initialization of a 2D ASM via our MRS-based clustering scheme resulted in an average overlap accuracy (true positive ratio) of 0.60, while the scheme of Cosio yielded a corresponding average accuracy of 0.56 over 388 2D MR image sections. During an ASM segmentation, using no initialization resulted in an overlap of 0.53, using the Cosio based methodology resulted in an overlap of 0.60, and using the MRS-based methodology resulted in an overlap of 0.67, with a paired Student's t-test indicating statistical significance to a high degree for all results. We also show that the final ASM segmentation result is highly correlated (as high as 0.90) to the initialization scheme.

*Corresponding author. Address: 599 Taylor Road Piscataway, NJ 08854, USA. Tel.: +1 732 445 4500x6213; fax: +1 732 445 3753. anantm@rci.rutgers.edu (A. Madabhushi)..

Keywords

Prostate segmentation; Active shape models (ASMs); Magnetic resonance spectroscopy (MRS); *In vivo* MRI; Spectral clustering

1. Introduction

Prostatic adenocarcinoma (CaP) is the second leading cause of cancer related deaths among men in the United States, with an estimated 186,000 new cases in 2008 (Source: *American Cancer Society*). The current standard for detection of CaP is transrectal ultrasound (TRUS) guided symmetrical needle biopsy, which has a high false negative rate associated with it (Catalona, 1991). Recently, multi-modal Magnetic Resonance (MR) Imaging (MRI) comprising both structural T2-weighted (T2-w) MRI (Madabhushi et al., 2005; Zhu et al., 2003) and MR Spectroscopy (MRS) (Kurhanewicz et al., 1996, 2002; Kumar et al., 2008; Vilanova and Barcelo, 2007; Hom et al., 2006; Tiwari et al., 2009; Zaider et al., 2000; Kim et al., 2003; Coakley et al., 2003) have emerged as promising modalities for early detection of CaP (Kumar et al., 2008; Vilanova and Barcelo, 2007). MRS measures the relative concentrations of different biochemicals and metabolites in the prostate, and changes in relative concentrations of choline, creatine, and citrate are highly indicative of the presence of CaP. It is important to note that MRS acquisition has a lower resolution than MRI acquisition, and thus each MRS metavoxel (containing a spectral signal) is approximately 13 times the size of an MRI voxel (containing a single intensity value).

An example of a MR spectra signature associated with a T2-w MRI image is show in Fig. 1. The spectra corresponding to three metavoxels within the prostate are shown in red, and three spectra corresponding to metavoxels outside the prostate are shown in cyan. The average spectra of the extra-prostatic metavoxels is shown in Fig. 1h as a blue line, and the average spectra of the prostatic metavoxels is shown as a red line. It can be seen that the prostatic MRS spectra are greatly different from the extra-prostatic MRS spectra. Finally, in Fig. 1i a scatter plot of the MRS spectra for a given slice is shown, in which the prostatic spectra are indicated by red dots and the extra-prostatic spectra are indicated by blue dots. To visualize the 256-dimensional spectra in three dimensions, principal component analysis was used. This scatter plot shows an example of how the prostatic and extra-prostatic spectra are distinct.

As of 2009, there are approximately 16 ongoing clinical trials in the US aiming to demonstrate the role of MR in a diagnostic, clinical setting.[1] Recent literature suggests that the integration of MRI and MRS could potentially improve sensitivity and specificity for CaP detection (Hom et al., 2006). In fact, when combined with MRI, using MRS data could yield prostate cancer detection specificity and sensitivity values as high as 90% and 88% respectively (Testa et al., 2007). Recently, computer-aided diagnosis (CAD) schemes have emerged for automated CaP detection from prostate T2-w MRI (Madabhushi et al., 2005; Chan et al., 2003) and MRS (Tiwari et al., 2007, 2008, 2009). In Tiwari et al. (2009), we showed that spectral clustering of the MRS data could be used to distinguish between prostatic and extra-prostatic voxels with accuracies as high as 98%. This paper improves upon the methodology presented in Tiwari et al. (2009) to drive a segmentation scheme for the prostate capsule on T2-w MRI.

With the recent advancements of prostate MR imaging, several prostate segmentation schemes have been developed (Zhu et al., 2003; Chiu et al., 2004; Costa et al., 2007; Ladak

---

[1]Source: www.clinicaltrials.gov.

et al., 2000; Hu et al., 2003; Pathak et al., 2000; Gong et al., 2004; Cosio, 2008; Gao et al., 2010). Segmentation of the prostate is useful for a number of tasks, including calculating the prostate volume pre- and post-treatment (Hoffelt et al., 2003; Kaminski et al., 2002), for creating patient specific anatomical models (Nathan et al., 1996), and for planning surgeries by helping to determine just how far outside the capsule they might need to go in order to capture any possible extra-capsular spread of the tumor. Additionally, identifying the prostate capsule is clinically significant for determining whether extra-capsular spread of CaP has occurred. Manual segmentation of the prostate, however, is not only laborious, but is also subject to a high degree of inter-, and intra-observer variability (Warfield et al., 2002, 2004). The aim of this work is to automatically identify the spectra within the prostate in order to initialize a multi-feature active shape model (ASM) for precise segmentation of the prostate capsule.

2. Previous work and motivation

Previous work on automatic or semi-automatic prostate segmentation has been primarily for transrectal ultrasound (TRUS) images (Chiu et al., 2004; Ladak et al., 2000; Hu et al., 2003; Pathak et al., 2000; Gong et al., 2004; Cosio, 2008). Ladak et al. (2000) and Hu et al. (2003) presented semi-automated schemes in which several points on the prostate contour are manually selected to initialize a deformable model for prostate segmentation. Manual intervention is then used to guide the segmentation. Pathak et al. (2000) similarly presented an algorithm to detect prostate edges which were then used as a guide for manual delineation on prostate ultrasound images. In Gong et al. (2004), deformable ellipses were used as the shape model to segment the prostate from TRUS images. Recently, some researchers have attempted to develop prostate segmentation methods from *in vivo* endorectal prostate MR imagery (Costa et al., 2007; Gong et al., 2004; Flores-Tapia et al., 2008; Makni et al., 2008; Liu et al., 2009; Betrouni et al., 2008; Klein et al., 2008; Zwiggelaar et al., 2003; Gao et al., 2010). Klein et al. (2008) presented a segmentation algorithm in which the prostate boundary is obtained by averaging the boundary of a set of training images which are best registered to a test image. Costa et al. (2007) presented a 3D method for segmenting the prostate and bladder simultaneously to account for inter-patient variability in prostate appearance. In Zwiggelaar et al. (2003), polar transformations were used in conjunction with edge detection techniques such as non-maxima suppression to segment the prostate. A recent paper by Gao et al. (2010) uses a more advanced registration task to first align the prostate shapes, and hence creates a more accurate statistical shape model. The appearance of the prostate is learned using both the distance to the center of the prostate as well as the voxels' intensity information in a Bayesian framework, which showed very promising results on a number of studies. One possible limitation with some of these prostate segmentation schemes (Costa et al., 2007; Gong et al., 2004; Klein et al., 2008; Zwiggelaar et al., 2003) is in their inability to deal with variations in prostate size, shape, and across different patient studies. Further, some of these methods are often susceptible to MR image intensity artifacts including bias field inhomogeneity and image intensity non-standardness (Madabhushi et al., 2005, 2006; Madabhushi and Udupa, 2006).

A popular segmentation method is the active shape model (ASM), a statistical scheme that uses a series of manually landmarked training images to generate a point distribution model (Cootes et al., 1995). Principal component analysis (PCA) is then performed on this point distribution model to generate a statistical shape model (Cootes et al., 1995). A texture model is created near each landmark point of each training image, and the Mahalanobis distance between the test image and the training model is minimized to identify the boundary of an object (Cootes et al., 1995; Cootes and Taylor, 1994, 2004). The Mahalanobis distance is a statistical distance measurement and routinely used in conjunction with ASMs to estimate dissimilarity between training and test image intensities at user

selected landmark points. After finding boundary points by minimizing the Mahalanobis distance, the shape model is deformed to best fit the boundary points, and the process is repeated until convergence.

While ASMs have been employed for a variety of different segmentation tasks related to biomedical imagery (Zhu et al., 2003, 2005; Cootes et al., 1993; Smyth et al., 1997; Montagnat and Delingette, 1997; de Bruijne et al., 2003; Mitchell et al., 2002), they have a major shortcoming in that they tend to be very sensitive to model initialization (Wang et al., 2002) and sometimes fail to converge to the desired edge. Manual initialization can be tedious and subject to operator variability. Over the last few years, some researchers have been exploring schemes for accurate and reproducible initialization of ASM's (Cosio, 2008; Brejl et al., 2000; Cootes et al., 1994). Seghers et al. (2007) presented a segmentation scheme where the entire image is searched for landmarks. They however concede that accurately initialized regions of interest (ROIs) would greatly improve their algorithm's efficiency and accuracy. Gao et al. (2010) use a single user click to initialize their prostate segmentation scheme, and would undoubtedly benefit from an automatic method for localizing the prostate in MR imagery. van Ginneken et al. (2002) pointed out that without *a priori* spatial knowledge of the ROI, very computationally expensive searches would be required for ASM initialization, contributing to a slow overall convergence time. Multi-resolution ASMs have also been proposed, wherein the model searches for the ROI in the entire scene at progressively higher image resolutions (Cootes et al., 1994). Brejl et al. (2000) presented a shape-variant Hough transform to initialize an ASM, but the scheme can be very computationally expensive. Cosio (2008) presented an ASM initialization method based on pixel classification which was applied to segmenting TRUS prostate imagery. The method employs a Bayesian classifier to discriminate between prostate and non-prostate pixels in ultrasound imagery. A trained prostate shape is then fit to the edge of the prostate, identified via the Bayesian classifier. A Genetic Algorithm (Mitechel, 1998) is employed to minimize the distance between the trained prostate shape and the edge of the prostate.

The second major shortcoming of ASM's is their inability to converge to the desired object boundary in the case of weak image gradients. The appearance model normally uses the intensities of the image to learn a statistical appearance model. However, there have been several studies in which using statistical texture features and more advanced appearance models have shown to yield improved accuracy over just using image intensities (Zhu et al., 2005; Seghers et al., 2007; van Ginneken et al., 2002; Toth et al., 2008, 2009). In addition, since the ASM models the object border using a multi-dimensional Gaussian, a large number of training images are required for accurate model generation (Ledoit and Wolf, 2004).

In this paper we present a novel, fully automated ASM initialization scheme for segmentation of the prostate on multi-protocol *in vivo* MR imagery by exploiting the MR spectral data. Note that for the studies considered in this work, the MRS data was acquired as part of routine multi-protocol prostate MR imaging and not specifically for the purposes of this project. While the resolution of MR and MRS data are different, the identification of prostate spectra by eliminating non-informative spectra outside the prostate provides an initial accurate ROI for the prostate ASM. We leverage the idea first introduced in Tiwari et al. (2008, 2009), in which spectral clustering was employed to distinguish between prostatic and extra-prostatic spectra. We achieve this through replicated *k*-means clustering of the MR spectra in the midgland. Replicated *k*-means clustering aims to overcome limitations associated with the traditional *k*-means algorithm (sensitivity to choice of initial cluster centers). For each slice, the largest cluster (identified as the non-informative cluster) is eliminated. The mean shape of the prostate is then transformed to fit inside the remaining spectra, which serves to provide the initial landmark points for a 2D ASM. In addition, since

the spectral data severely degrades away from the mid-gland of the prostate, we limit the clustering to the midgland. The resulting initialized shape is then rescaled to account for the change in size of the gland towards the base and the apex.

The ASM is performed in 2D because our limited number of 3D studies (32 in total) would prevent accurate statistical models from being generated in 3D. However, while we only had access to 32 3D studies, this constituted a total of 388 2D image slices. According to Ledoit and Wolf (2004), the ratio of the number of Gaussian dimensions (in our case 5) to the number of samples (in our case either 388 or 32) must be significantly less than 1. We therefore reasoned that while 32 3D samples would be insufficient to create an accurate 3D appearance model, the 388 slices would suffice to generate an accurate 2D statistical appearance model. In addition, we have opted to use multiple statistical texture features to better detect the prostate border. Statistical texture features have been shown to improve ASM accuracy (Seghers et al., 2007; van Ginneken et al., 2002; Toth et al., 2008, 2009). We calculate gray level statistics (such as mean and variance) of the neighborhood surrounding each landmark on the prostate border and use these statistics to generate our appearance model.

Note that as in traditional ASM schemes, the off-line training phase needs to only be done once. In this paper we compare the ASM segmentation performance using our MRS-based initialization scheme against corresponding results obtained via the initialization method recently presented by Cosio (2008). In Cosio (2008), only four patients were evaluated, with a total of 22 TRUS image slices, resulting in a mean MAD value of 1.65 mm. Note that while the Cosio method was originally presented for US data, in this work, we evaluate it in the context of prostate MR imagery.[2] The popular Cootes et al. (1995) ASM was employed with both initialization schemes. Both schemes were rigorously evaluated via a 5-fold randomized cross validation system, in which the manual delineations of the prostate by an expert radiologist were used as the surrogate for ground truth. We also rigorously evaluted the results of the replicated k-means clusteirng algorithm with the results from two other popular clustering schemes – hierarchical and mean-shift clustering.

The rest of the paper is organized as follows. In Section 3 we provide a brief overview of our MRS-based ASM initialization scheme. In Section 4 we present the details of our methodology for identifying the prostate ROI via spectral clustering of MRS data. Section 5 describes the methodology for our ASM segmentation system. Section 6 describes the experimental set up and evaluation methods, in addition to our implementation of the ASM initialization method by Cosio (2008). In Section 7 we present both the qualitative and quantitative results, followed by a brief discussion of our findings. Finally, concluding remarks and future directions are presented in Section 8.

3. System overview

3.1. Notation

We define a spectral scene $\widehat{\mathscr{C}} = \left(\widehat{C}, \widehat{F} \right)$ where $\widehat{C}$ is a 2D grid of metavoxels. Note that metavoxel is a voxel at the lower spectral resolution. For each spatial location $\widehat{c} \in \widehat{C}$, there is an associated 256-dimensional valued spectral vector $\widehat{F}(\widehat{c}) = \left[\widehat{f_j}(\widehat{c}) \, | \, j \in \{1, \dots, 256\} \right]$, where $\widehat{f_j}(\widehat{c})$ represents the concentration of different biochemicals (such as creatine, citrate, and choline). We define the associated T2-w MR intensity image scene $\mathscr{C} = (C, f)$, where C represents a set of spatial locations (voxels), $f(c)$ is the MR image intensity function

---

[2]The extension of the scheme in Cosio (2008) to MR imagery was made possible by the lead author (Cosio) of Cosio (2008).

associated with every $c \in C$, and $c = (x_c, y_c)$. The distance between any two adjacent metavoxels, $\widehat{c}, \widehat{d} \in \widehat{C}, \|\widehat{c} - \widehat{d}\|_2$ (where $\|\cdot\|_2$ denotes the L_2 norm) is roughly 13 times the distance between any two adjacent spatial voxels $c, d \in C$. We define $\mathbf{X} = \{c_1 \ldots c_N\} \subset C$ as the set of N landmarks used to define a given prostate shape. The mean landmark coordinates across all training images is given as $\bar{\mathbf{X}} = \{\bar{c}_1, \ldots, \bar{c}_N\}$. The κ-neighborhood of pixels surrounding each $c \in C$ is denoted as $\mathcal{N}_\kappa(c)$, where for $\forall d \in \mathcal{N}_\kappa(c), \|d - c\|_2 \leq \kappa$, $c \notin \mathcal{N}_\kappa(c)$. Finally, we denote as $\Delta \in \{MRS, Cos\}$ the MRS-based ASM presented in this work and the Cosio method (Cosio, 2008) respectively. A table of commonly used notation and symbols employed in this paper is shown in Table 1.

3.2. Data description

Our data comprises 32 multi-protocol clinical prostate MR datasets including both MRI and MRS endorectal *in vivo* data. These were collected during the American College of Radiology Imaging Network (ACRIN) multi-site trial (Mr imaging, xxxx) and from the University of California, San Fransisco. The MRS and MRI studies were obtained on 1.5 Tesla MRI scanners, and the MRI studies were axial T2-w images. The 32 3D studies comprised a total of 388 2D slices, with a spatial XY resolution of 256×256 pixels, or 140×140 mm. The ground truth for the prostate boundary on the T2-w images was obtained by manual outlining of the prostate border on each 2D section by a solitary expert radiologist, one with over 10 years of experience in prostate MR imagery.

3.3. Brief outline of ASM initialization schemes

Fig. 2 illustrates the modules and the pathways comprising our automated initialization system. First, replicated k-means clustering is performed on the spectra in the midgland, identified as the middle slices. The largest cluster obtained is identified as the non-informative cluster corresponding to the extra-prostatic spectra and removed. The remaining spatial locations corresponding to the resulting spectra are denoted by S_{MRS}. The prostate shape is fit to the region corresponding to these informative spectra. The clustering results are then extended to the base and apex slices.

4. Methodology for MRS-based ASM initialization scheme

4.1. Clustering of spectra (calculation of S_{MRS})

The crux of the methodology is to determine a set of prostate voxels (S_{MRS}) based on a clustering of the spectroscopic data. This algorithm is described in the form of a sequence of steps below.

1. For a given 2D MRS slice $\widehat{\mathscr{C}} = (\widehat{C}, \widehat{F})$, we first obtain the MR spectra

$$\widehat{F}(\widehat{c}) = \left[\widehat{f}(\widehat{c}) | j \in \{1, \ldots, 256\}\right].$$

2. The metavoxels $\widehat{c} \in \widehat{C}$, are aggregated into k clusters $V_a \subset \widehat{C}, a \in \{1, \ldots, k\}$, by applying k-means clustering to all $\widehat{F}(\widehat{c}), \forall \widehat{c} \in \widehat{C}$. k-means clustering aims to minimize the sum of distances to the clusters' centroids, for all clusters. Formally, it iteratively estimates

$$\underset{V_1, \ldots, V_k}{\arg\min} \sum_{a=1}^{k} \sum_{\widehat{c} \in V_a} \left\| \widehat{F}(\widehat{c}) - \frac{1}{|V_a|} \sum_{\widehat{c} \in V_a} \widehat{F}(\widehat{c}) \right\|_2. \quad (1)$$

3. Since the *k*-means algorithm is dependent on the starting locations of the centroids (i.e. which V_a each $\hat{c}$ initially belongs to), the result is sometimes a local minima instead of a global minima. To overcome this limitation, the clustering was repeated 25 times with random initial locations of the centroids, and the resulting clustering which yields the minimum value from Eq. (1) is selected. Repeating the clustering more than 25 times did not significantly change the results.

4. The dominant cluster is identified as being extra-prostatic (non-informative), and the metavoxels in this cluster are removed. This is akin to the approach used in Tiwari et al. (2009), in which it was found that the dominant cluster is the non-informative cluster. The set of remaining metavoxels is then defined as,

$$\widehat{S}_{MRS} = \left\{ \widehat{c} \,|\, \widehat{c} \in V_a, a \neq \underset{a}{\operatorname{argmax}} |V_a| \right\}. \quad (2)$$

The set of MRI voxels corresponding to metavoxels in $\widehat{S}_{MRS}$ are then idenfitied. For our data, we found that $k = 3$ clusters yielded the best results. Fig. 3a shows the 3 clusters $V_1 - V_3$ as colored metavoxels. The largest cluster is shown in green, and would be eliminated, yielding $\widehat{S}_{MRS}$ as the cluster comprising blue and red metavoxels. While $\widehat{S}_{MRS}$ denotes the set of metavoxels, the voxels associated with $\widehat{S}_{MRS}$ are denoted as S_{MRS} and are shown in red[3] in Fig. 3b.

4.2. Fitting the prostate shape (calculation of $\mathbf{X}^0$)

Cosio (2008) employed the Genetic Algorithm to optimize the pose parameters of the prostate shape to fit a given binary mask. We found that using the objective function described below yielded an accurate initialization for a given set of prostate pixels S_{MRS}. The mean shape $\overline{\mathbf{X}}$ constitutes a polygon, and the set of voxels inside this polygon is denoted as $S_{\overline{\mathbf{X}}}$. More generally, for a given set of affine transformations T, which represent scaling rotation and translation, the set of voxels within that polygon are denoted as $S_{T(\overline{\mathbf{X}})}$. The objective function we use aims to maximize the true positive ratio, so that the initialization is given as

$$\mathbf{X}_\Delta^0 = T\left(\overline{\mathbf{X}}\right), \quad \text{where} \quad T = \underset{T}{\operatorname{argmax}} \left[\frac{S_\Delta \cap S_{T(\overline{\mathbf{x}})}}{S_\Delta \cup S_{T(\overline{\mathbf{x}})}} \right], \quad (3)$$

where $\Delta \in \{MRS, Cos\}$. The optimization of Eq. (3) is performed via the Genetic Algorithm (Mitechel, 1998). The entire initialization process for $\Delta = MRS$ is shown in Fig. 3.

4.3. Estimation of $\mathbf{X}_{MRS}^0$ in the base and apex

The MRS spectra lose their fidelity towards the base and the apex of the prostate. This is demonstrated in Fig. 4a, in which the three resulting clusters ($V_1, \ldots, V_3$) are shown via red, green, and blue metavoxels respectively. It was found that the spectra in the midgland of the prostate yielded accurate estimations of S_{MRS}. For this reason, we perform our clustering algorithm in the midgland of the prostate, the results of which are then extended to the base and apex. Note that since the 2D T2-w MRI slices tend to cover the prostate from base to apex, we have found that in our studies, the middle slice typically corresponded to the midgland. Hence we used the middle slice as our anchor midgland slice. We observed that the area of the prostate decreases to 80% its size in the base, and 30% its size in the

---

[3]For interpretation of color in 'Figs. 1–10', the reader is referred to the web version of this article.

apex. Fig. 4b demonstrates this tapering off of the gland in the base and apex. Fig. 4b is a histogram showing the size of the prostate relative to the central slice for all ground truth segmentations. Hence, to calculate $\mathbf{X}^0_{MRS}$ for the remaining slices, $\mathbf{X}^0_{MRS}$ is first calculated for slice 5, and is linearly scaled down to 80% its size for the first third of the 2D sections, and to 30% its size for the latter third of the gland.

5. Multi-feature ASM based segmentation

5.1. Basic shape model

Following model initialization $\left(\mathbf{X}^0_\Delta\right)$, an ASM search (Cootes et al., 1995) is performed to segment the prostate from a new image. An ASM is defined by the equation

$$\mathbf{X}=\overline{\mathbf{X}}+\mathbf{P}\cdot\mathbf{b}, \quad (4)$$

where $\overline{\mathbf{X}}$ represents the mean shape, $\mathbf{P}$ is a matrix of the first few principal components (Eigenvectors) of the shape, created using Principal Component Analysis (PCA), and $\mathbf{b}$ is a vector defining the shape, which can range from between –3 and +3 standard deviations from the mean shape. Therefore, $\mathbf{X}$ is defined by the variable $\mathbf{b}$. Given a set of landmark points $\mathbf{X}^i_\Delta$, ($\Delta \in \{$ MRS, Cos $\}$) for iteration i, the goal is to find landmark points $\widehat{\mathbf{X}}^i$ closest to the object border. The shape is then updated using Eq. (4) where

$$\mathbf{b}=\mathbf{P}^T\cdot\left(\widehat{\mathbf{X}}^i - \mathbf{X}^i\right), \quad (5)$$

where each element of $\mathbf{b}$ can only be within ±3 standard deviations of the mean shape. The final ASM segmentation is denoted as $\mathbf{X}^{Final}_\Delta$. The training of the ASM to determine $\overline{\mathbf{X}}$ and $\mathbf{P}$ is performed by manual delineation of the prostate boundary followed by manual alignment of 100 equally spaced landmark points along this boundary ($N = 100$). It should be noted that this needs to only be performed once in an off-line setting, and once an ASM is trained it can be used for repeated segmentations without significant manual intervention.

5.2. Basic appearance model

We define the set of intensity values near c as $\mathbf{g}(c) = \{f(d)|d \in \mathcal{N}_\kappa(c)\}$. Over all training images, the mean intensity values for a given landmark point c_n, $n \in \{1, \ldots, N\}$, are denoted as $\bar{\mathbf{g}}_n$, with the covariance matrix denoted as Σ_n. We define the set of pixels near $c_n \in \mathbf{X}^i$ along the normal to the shape as $\widehat{\mathcal{N}}(c_n)$. The standard cost function for a given pixel to the training set is the Mahalanobis distance. Therefore, $\widehat{\mathbf{X}}^i$ is defined as

$$\widehat{\mathbf{X}}^i = \{d_n|n \in \{1, \ldots N\}\}, \quad \text{where} \quad d_n$$
$$=\underset{e\in\widehat{\mathcal{N}}(c_n)}{\operatorname{argmin}}\left[\left(\mathbf{g}(e) - \bar{\mathbf{g}}_n\right)^T\cdot\Sigma_n^{-1}\cdot\left(\mathbf{g}(e) - \bar{\mathbf{g}}_n\right)\right]. \quad (6)$$

5.3. Multi-feature appearance model

Our previous work and that of others in employing multiple image features to drive the ASM model has shown that multi-feature ASM's are more likely to latch on to weak edges and boundaries compared to the traditional intensity driven ASM (Seghers et al., 2007; van Ginneken et al., 2002; Toth et al., 2008, 2009). In this work, in addition to using image intensity values $\mathbf{g}(c)$, we also extracted the mean, standard deviation, range, skewness, and kurtosis of intensity values with local neighborhoods associated with every $c \in C$. If E

represents the expected value of an image feature, then the feature vector ($\mathbf{G}(c)$) associated with each $c \in C$ is defined as,

$$\mathbf{G}(c) = \left\{ \bar{\mathbf{g}}(c), E\left[\left(\mathbf{g}(c) - \bar{\mathbf{g}}(c)\right)^2\right]^{1/2}, \max \mathbf{g}(c) - \min \mathbf{g}(c), \frac{E\left[\left(\mathbf{g}(c) - \bar{\mathbf{g}}(c)\right)^3\right]}{E\left[\left(\mathbf{g}(c) - \bar{\mathbf{g}}(c)\right)^2\right]^{3/2}}, \frac{E\left[\left(\mathbf{g}(c) - \bar{\mathbf{g}}(c)\right)^4\right]}{E\left[\left(\mathbf{g}(c) - \bar{\mathbf{g}}(c)\right)^2\right]^2} \right\}. \quad (7)$$

Our cost function in Eq. (6) thus uses $\mathbf{G}$ instead of $\mathbf{g}$.

6. Experiments and performance measures

6.1. Performance measures

For each image, a single expert radiologist segmented the prostate region, yielding ground truth landmarks $\mathbf{X}_E$. For a given shape $\mathbf{X}$, the set of pixels contained within the shape is denoted as $S_\mathbf{X}$. We employ the performance measures shown in Table 2.

Performance measures 1–4 are area based performance measures, in which a higher value indicates a more accurate segmentation, while performance measures 5 and 6 are edge based performance measures which evaluate proximity of the ASM extracted boundary compared to the manually delineated boundary. A lower value in measures 5 and 6 reflects a more accurate segmentation.

6.2. Comparison of clustering algorithms

We compared the efficacy of the replicated k-means clustering scheme with hierarchical clustering (Hastie et al., 2009) and mean-shift clustering (Comaniciu and Meer, 2002). Hierarchical clustering generates a dendrogram based off the Euclidean distance between spectra, and hierarchically combines spectra which have a low distance between them into a single cluster. The process is repeated until a pre-specified number of clusters remain (Hastie et al., 2009). Mean-shift clustering attempts to iteratively learn the density of the feature space and yields a clustering result based of the manifold instead of a pre-specified number of clusters (Comaniciu and Meer, 2002). Each methodology was used to calculate S_{MRS} in the midgland, and these estimations of $\mathbf{X}_{MRS}^0$ in the midgland were compared to the ground truth segmentations $\mathbf{X}_E$ for all studies. Table 3 summarizes the clustering experiments performed.

6.3. Comparison of initialization methods

6.3.1. Cosio based initialization (calculation of $\mathbf{X}_{Cos}^0$)—Cosio developed an automated ASM initialization scheme (Cosio, 2008) to segment prostate ultrasound images. We extended the Cosio (2008) scheme to MR imagery in order to compare this scheme against our MRS-based initialization method.[4] The crux of the methodology is to classify the pixels in the images based on a Bayesian classification scheme using a mixture of Gaussians to represent the distribution of prostate and non-prostate pixels.

1. A set of 10 images was expertly segmented, resulting in a set of voxels within the prostate, denoted as $S_+ \subseteq C$ and a set of pixels outside the prostate, denoted as $S_- = C - S_+$.

---

[4]Extension of the scheme in Cosio (2008) to MR imagery was performed with the assistance of the first author in Cosio (2008), Fernando Cosio

2. Each voxel $c = (x_c, y_c)$ had a three dimensional vector constructed from its x and y coordinates and its intensity value $F_{xy}(c) = [x_c, y_c, f(c)]$.

3. The distribution for prostate pixels $(\mathscr{D}_+)$ and non-prostate pixels $(\mathscr{D}_-)$ based on the spatial-intensity vector $F_{xy}(c) = [x_c, y_c, f(c)]$ was then estimated by using the Expectation–Maximization function to generate a mixture of 10 Gaussians. The distribution is given as $\mathscr{D} \sim \sum_{b=1}^{10} N\left(\mu_b, \sigma_b^2\right)$, where N is a 3-D normal distribution such that $\mu_b \in \Re^3$ and $\sigma_b^2 \in \Re^{3 \times 3}$.

4. For each of the images considered, Bayes' law (Duda et al., 2001) was then used to determine the posterior conditional probabilities of a given voxel $c \in C$ belonging to the prostate class $(P(w_+|c, \mathscr{D}_+))$ and the non-prostate class $(P(w_-|c, \mathscr{D}_-))$, where w denotes the class. The set of pixels S_{Cos} represents those pixels in which the likelihood of belonging to the prostate class was greater than the likelihood of being part of the non-prostate class, so that

$$S_{Cos} = \{c | \ln(P(w_+|c, \mathscr{D}_+)) + \ln(P(w_+)) > \ln(P(w_-|c, \mathscr{D}_-)) + \ln(P(w_-))\}. \quad (8)$$

The methodology presented in Section 4.2 was then used to calculate $\mathbf{X}_{Cos}^0$.

6.3.2. Comparing ASM segmentations using different initialization schemes—

To test the ASM, each initialization method ($\Delta \in \{MRS, Cos\}$) resulted in an initialization $\mathbf{X}_\Delta^0$ for each image, and 2a final ASM segmentation $\mathbf{X}_\Delta^{Final}$. To evaluate ASM performance in the absence of any automated initialization, we placed the mean prostate shape in the center of the image yielding a third initialization, $\Delta = Mid$. A 5-fold cross validation was performed as follows. The 32 3D studies were randomly split into five groups of about six studies. For each group of studies, the remaining 26 were used for training the ASM, and the segmentation was performed for each slice in each of the six studies. This was repeated for each group resulting in segmentations for all 388 images. The segmentations were compared to the ground truth $\mathbf{X}_E$ in terms of the six performance measures in Table 2. A paired Student's t-test was then carried out for each of the performance measures to determine the level of statistical significance. The t-test was performed over all 388 images (or, stated differently, with 387 degrees of freedom). Finally, the correlation (R^2 value) between each final segmentation result $\left(\mathbf{X}_\Delta^{Final}, \Delta \in \{MRS, Cos, Mid\}\right)$ and the initialization result was calculated for each performance measure, to determine the correlation between the final segmentation with respect to the initialization. A high R^2 value would indicate that the model is very sensitive to the initialization.

6.4. Comparison of multi-resolution ASM's

For each of the initialization methods ($\Delta \in \{MRS, Cos, Mid\}$), a multi-resolution ASM was also performed. A Gaussian image pyramid was constructed with 4 image resolution levels (ranging from 32×32 pixels to 256×256 pixels), and at each image level a distinct ASM model is constructed. The result from the final pyramid (the full-resolution image) was used as $\mathbf{X}_\Delta^{Final}$, and 5-fold cross validation and statistical significance tests were performed as described above. Finally, the correlation (R^2 value) was also calculated, the hypothesis being that if the multi-resolution framework was able to overcome poor or lack of initialization, then the R^2 values would be lower for the multi-resolution experiments. In essence, we were aiming to explore whether a multi-resolution approach would make redundant the need for initialization. The entire set of ASM experiments performed are summarized in Table 4.

7. Results and discussion

7.1. Comparison of clustering algorithms $(\mathscr{E}_1 - \mathscr{E}_3)$

Fig. 5 shows some qualitative results from $\mathscr{E}_1 - \mathscr{E}_3$ for a midgland slice, which was used to calculate S_{MRS}. In all the images, the red cluster indicates the largest cluster which is removed, so that $\widehat{S}_{MRS}$ corresponds to all metavoxels that are not red. While all the clustering methodologies found a set of metavoxels within the prostate, it is obvious that only the replicated k-means clustering algorithm was able to properly identify most of the prostate metavoxels. The superior performance of replicated clustering over the two other algorithms might have to do with the fact that we were unable to identify the optimal parameter values for the mean-shift and hierarchical clustering schemes. Although we experimented with several different parameter settings, the hierarchical and mean-shift clustering algorithms ended up clustering most of the background metavoxels with the prostate metavoxels. The replicated k-means clustering, however was able to group most of the prostate metavoxels together for a value of $k = 3$. Note that $k = 3$ appeared to work better than $k = 2$, owing perhaps to some heterogeneity of tissues (cancerous and benign areas) within the prostate.

For each of the 32 studies, $\mathbf{X}^0$ was calculated for the midgland slice, and compared to $\mathbf{X}_E$. The quantitative results for a single midland slice are shown in Fig. 7 over all 32 studies. The most important thing to note is the extremely high sensitivity of the replicated k-means compared to the other clustering algorithms, suggesting that the mean-shift and hierarchical clustering tended to under-segment the prostate voxels. In addition, the overlap measure of the replicated k-means, which takes into account both false positive and false negative pixels, was higher than any of the other algorithms, suggesting a more accurate overall initialization.

7.2. Comparison of initialization schemes $(\mathscr{E}_4, \mathscr{E}_5, \mathscr{E}_7, \mathscr{E}_8, \mathscr{E}_{10}, \mathscr{E}_{11})$

Fig. 6 shows S_Δ in red with $\mathbf{X}_\Delta^0$ in white for $\Delta \in \{Cos, MRS\}$ for two different studies, with $\mathbf{X}_E$ shown in the third column ((c) and (f)) for reference. It can be seen that both perform quite well in locating the prostate pixels. This was further tested quantatitively over all 388 slices, results of which are shown in Fig. 8. Fig. 8 illustrates that in many cases the MRS initialization yielded superior results. It should be noted that the specificity was extremely high in most cases due to the large size of the image compared to the size of the target object $(|C| = \gg |S_x|)$. Our model yielded an average value of while the Cosio method had a value of 0.62. Comparison of our segmentation system with other MR prostate segmentation schemes show that our system performs comparably to other related techniques. Zhu et al. (2003) have overlap coefficients ranging from about 0.15 to about 0.85, while our mean overlap is 0.66. Costa et al. (2007) used prior knowledge from the MRI scan to localize an ROI containing the prostate, resulting in a mean sensitivity and PPV of 0.75 and 0.80 respectively for the prostate. Our model achieved mean sensitivity and PPV values of 0.81 and 0.79 respectively. Comparing the initialization schemes $\left(\mathbf{X}_\Delta^0, \Delta \in \{MRS, Cos, Mid\}\right)$ revealed that all results were statistically significant to a high degree, except for the edge based performance measures between $\Delta = MRS$ and $\Delta = Mid$, shown in Table 5. When comparing the actual ASM segmentations, all results were statistically significant except for the Hausdorff distance between $\Delta = Cos$ and $\Delta = Mid$, shown in Table 6. In Table 8, it can be seen that the ASM is extremely sensitive to the initialization, with the lowest R^2 value being 0.71.

7.3. Comparison of multi-resolution ASM's $(\mathscr{E}_6, \mathscr{E}_9, \mathscr{E}_{12})$

Fig. 9 shows the result from the multi-resolution ASM's over 388 images using a 5-fold cross validation scheme. These results were then compared to the values reported in Fig. 8b via the use of a statistical significance test, shown in Table 7. Apart from a few scenarios (sensitivity of $\Delta = MRS$, specificity of $\Delta = Cos$, and overlap and edge performance measures of $\Delta = Mid$), the multi-resolution approach generally improved the ASM segmentation results significantly. Finally, the R^2 values from the multi-resolution experiments were calculated, and they were all extremely high (with the lowest being 0.59). It is interesting that in the Δ MRS experiments, the R^2 values actually increased with the multi-resolution framework, and additional studies will have to be carried out to investigate this further. Overall, while a multi-resolution framework is useful for accurate segmentations, the fact that the multi-resolution results were still correlated to the initialization suggests that a multi-resolution framework by itself is not sufficient for addressing the lack of accurate model initialization.

In addition, Table 9 shows that while the Cosio scheme was very efficient, the MRS initialization scheme only required approximately 1 second to accurately initialize the prostate ROI (using a 2.8 GHz, 32 GB RAM system with MATLAB 2009b and the Ubuntu Linux operating system). In a clinical setting, the need for rapid initialization of a segmentation scheme is motivated by the need for real time biopsy guidance, real time registration of ultrasound with MRI, and radiation therapy applications, all of which use segmentation of the prostate gland as a first step (Barqawi et al., 2007; Chen et al., 2010; Zhou et al., 2010).

8. Concluding remarks

In this paper, we have presented a fully automated and accurate ASM initialization scheme for prostate segmentation from multi-protocol *in vivo* MRI/MRS data. With the increasing use of MR imaging of the prostate, several institutions are beginning to acquire multi-modal MR prostate data, including MR spectroscopy (Kurhanewicz et al., 1996; Kumar et al., 2008; Vilanova and Barcelo, 2007; Hom et al., 2006; Tiwari et al., 2009). The primary novel contribution of our work is in leveraging information from one imaging protocol (spectroscopy) to drive the segmentation of the prostate on a different protocol (T2-weighted structural MRI). To the best of our knowledge this is the first instance of multi-modal information being used in this fashion for ASM initialization. Our method uses replicated *k*-means clustering to cluster the MRS spectra in the midgland. For the studies we considered, the central slice was ssumed to be the midgland. This may not always be the case, and future work will entail developing an automated, more intelligent scheme for selecting the midgland slice. We then eliminate the background spectra, fit the shape to the remaining spectra, and extend our initializations to the base and apex of the prostate. We employed a multi-feature ASM to perform the segmentation, wherein multiple statistical texture features were used to complement image intensities. We compared our MRS initialization method against a recent image feature driven ASM inititialization method by Cosio (2008) and found that our scheme resulted in significantly better segmentations. Future work will entail evaluating our scheme on a larger cohort of data.

Acknowledgments

References

Barqawi AB, Lu L, Crawford ED, Fenster A, Werahera PN, Kumar D, Miller S, Suri JS. Three different strategies for real-time prostate capsule volume computation from 3-D end-fire transrectal ultrasound. Conf. Proc. IEEE Eng. Med. Biol. Soc. 2007:816–818. [PubMed: 18002081]

Betrouni N, Dewalle AS, Puech P, Vermandel M, Rousseau J. 3D delineation of prostate, rectum and bladder on MR images. Computer Mediated Imaging and Graphics. 2008; 32(7):622–630.

Brejl M, Sonka M. Object localization and border detection criteria design in edge-based image segmentation: automated learning from examples. IEE Transactions on Medical Imaging. 2000; 19(10):973–985.

Catalona W. Measurement of prostate-specific antigen in serum as a screening test for prostate cancer. New England Journal of Medicine. 1991; 324(17):1156–1161. [PubMed: 1707140]

Chan I, William Wells I. Mulkern Robert V. Haker Steven, Zhang Jianqing, Zou Kelly H. Maier Stephan E. Tempany Clare M.C. Detection of prostate cancer by integration of line-scan diffusion, T2-mapping and T2-weighted magnetic resonance imaging; a multichannel statistical classifier. Medical Physics. 2003; 30(9):2390–2398. [PubMed: 14528961]

Chen T, Kim S, Goyal S, Jabbour S, Zhoy J, Rajagopal G, Haffty B, Yue N. Object-constrained meshless deformable algorithm for high speed 3d nonrigid registration between CT and CBCT. Medical Physics. 2010; 37(1):197–210. [PubMed: 20175482]

Chiu B, Freeman GH, Salama MMA, Fenster A. Prostate segmentation algorithm using dyadic wavelet transform and discrete dynamic contour. Physics of Medical Biology. 2004; 49(21):4943–4960.

Coakley FV, Qayyum A, Kurhanewicz J. Magnetic resonance imaging and spectroscopic imaging of prostate cancer. Journal of Urology. 2003; 170(6):S69–S76. [PubMed: 14610414]

Comaniciu D, Meer P. Mean shift: A robust approach toward feature space analysis. IEEE Transactions on Pattern Analysis and Machine Intelligence. 2002; 24(5):603–619.

Cootes TF, Taylor CJ. Using grey-level models to improve active shape model search. 1994. Conference A: Computer Vision and Image Processing, Proceedings of the 12th IAPR International Conference on Pattern Recognition. 1994; 1:63–67.

Cootes, TF.; Taylor, CJ. Statistical models of appearance for computer vision. 2004.

Cootes TF, Hill A, Taylor CJ, Haslam J. The use of active shape models for locating structures in medical images. IPMI. 1993:33–47.

Cootes TF, Taylor CJ, Lanitis A. Multi-resolution search with active shape models. Computer Vision and Image Processing. 1994; 1:610–612.

Cootes TF, Taylor CJ, Cooper DH, Graham J. Active shape models – their training and application. Computer Vision and Image Understanding. 1995; 61(1):38–59.

Cosio FA. Automatic initialization of an active shape model of the prostate. Medical Image Analysis. 2008; 12(4):469–483. [PubMed: 18346931]

Costa J, Delingette H, Novellas S, Ayache N. Automatic segmentation of bladder and prostate using coupled 3D deformable models. MICCAI. 2007:252–260. [PubMed: 18051066]

de Bruijne, M.; Ginneken, Bram van; Viergever, MA.; Niessen, WJ. Adapting Active Shape Models for 3D Segmentation of Tubular Structures in Medical Images. Vol. 2732. Springer; Berlin/ Heidelberg: 2003. p. 136-147.

Duda, RO.; Hart, PE.; Stork, DG. Pattern Classification. second ed.. Wiley-Interscience; 2001.

Flores-Tapia D, Thomas G, Venugopal N, McCurdy B, Pistorius S. Semi automatic MRI prostate segmentation based on wavelet multiscale products. Conf. Proc. IEEE Eng. Med. Biol. Soc. 2008:3020–3023. [PubMed: 19163342]

Gao Y, Sandhu R, Fichtinger G, Tannenbaum A. A coupled global registration and segmentation framework with application to magnetic resonance prostate imagery. IEEE Transactions on Medical Imaging. 2010

Gong L, Pathak SD, Haynor DR, Cho PS, Kim Y. Parametric shape modeling using deformable superellipses for prostate segmentation. IEE Transactions on Medical Imaging. 2004; 23(3):340–349.

Hastie, T.; Tibshirani, R.; Friedman, J. The Elements of Statistical Learning. Springer; 2009.

Hoffelt SC, Marshall LM, Garzotto M, Hung A, Holland J, Beer TM. A comparison of CT scan to transrectal ultrasound measured prostate volume in untreated prostate cancer. International Journal of Radiation Oncology and Biological Physics. 2003; 57(1):29–32.

Hom JJ, Coakley FV, Simko JP, Lu Y, Qayyum A, Westphalen ACA, Schmitt LD, Carroll PR, Kurhanewicz J. High-grade prostatic intraepithelial neoplasia in patients with prostate cancer: MR and MR spectroscopic imaging features – initial experience. Radiology. 2006; 242(2):483–489. [PubMed: 17179396]

Hu, Ning; Downey, Dónal B.; Fenster, Aaron; Ladak, Hanif M. Prostate boundary segmentation from 3D ultrasound images. Medical Physics. 2003; 30(7):1648–1659. [PubMed: 12906182]

Kaminski JM, Hanlon AL, Horwitz EM, Pinover WH, Mitra RK, Hanks GE. Relationship between prostate volume, prostate-specific antigen nadir, and biochemical control. International Journal of Radiation Oncology and Biological Physics. 2002; 52(4):888–892.

Kim H, Buckley DL, Peterson DM, Duensing GR, Caserta J, Fitzsimmons J, Blackband SJ. In vivo prostate magnetic resonance imaging and magnetic resonance spectroscopy at 3 Tesla using a transceive pelvic phased array coil: preliminary results. Investigative Radiology. 2003; 38(7):443–451. [PubMed: 12821859]

Klein S, van der Heide UA, Lips IM, van Vulpen M, Staring M, Pluim JPW. Automatic segmentation of the prostate in 3D MR images by Atlas matching using localized mutual information. Medical Physics. 2008; 35(4):1407–1417. [PubMed: 18491536]

Kumar R, Nayyar R, Kumar V, Gupta NP, Hemal AK, Jagannathan NR, Dattagupta S, Thulkar S. Potential of magnetic resonance spectroscopy imaging in predicting absence of prostate cancer in men with serum prostate-specific antigen between 4 and 10 ng/ml: a follow-up study. Technology and Engineering. 2008; 72(4):859–863.

Kurhanewicz J, Vigneron DB, Hricak H, Narayan P, Carroll P, Nelson SJ. Three-dimensional h-1 MR spectroscopic imaging of the in situ human prostate with high (0.24–0.7 cm^3) spatial resolution. Radiology. 1996; 198(3):795–805. [PubMed: 8628874]

Kurhanewicz J, Swanson MG, Nelson SJ, Vigneron DB. Combined magnetic resonance imaging and spectroscopic imaging approach to molecular imaging of prostate cancer. Journal of Magnetic Resonance Imaging. 2002; 16(4):451–463. [PubMed: 12353259]

Ladak HM, Mao Y, ad Wang F, Downey DB, Steinman DA, Fenster A. Prostate boundary segmentation from 2D ultrasound images. Medical Physics. 2000; 27(8):1777–1788. [PubMed: 10984224]

Ledoit O, Wolf M. A well-conditioned estimator for large-dimensional covariance matrices. Journal of Multivariate Analysis. 2004; 88(2)

Liu X, Langer DL, Haider MA, Van der Kwast TH, Evans AJ, Wernick MN, Yetik IS. Unsupervised segmentation of the prostate using MR images based on level set with a shape prior. Conf. Proc. IEEE Eng. Med. Biol. Soc. 2009; 1:3613–3616. [PubMed: 19964082]

Madabhushi A, Udupa JK. Interplay between intensity standardization and inhomogeneity correction in MR image processing. IEEE Transactions on Medical Imaging. 2005; 24(5):561–576. [PubMed: 15889544]

Madabhushi A, Udupa JK. New methods of MR image intensity standardization via generalized scale. Medical Physics. 2006; 33(9):3426–3434. [PubMed: 17022239]

Madabhushi A, Feldman MD, Metaxas DN, Tomaszeweski J, Chute D. Automated detection of prostatic adenocarcinoma from high-resolution ex vivo MRI. IEEE Transactions on Medical Imaginag. 2005; 24(12):1611–1625.

Madabhushi A, Udupa JK, Souza A. Generalized scale: theory, algorithms, and application to image inhomogeneity correction. Computer Vision and Image Understanding. 2006; 101(2):100–121.

Makni N, Puech P, Lopes R, Viard R, Colot O, Betrouni N. Automatic 3D segmentation of prostate in MRI combining a priori knowledge, Markov fields and Bayesian framework. Conf. Proc. IEEE Eng. Med. Biol. Soc. 2008:2992–2995. [PubMed: 19163335]

Mitchell SC, Bosch JG, Lelieveldt BPF, van der Geest RJ, Reiber JHC, Sonka M. 3-D active appearance models: segmentation of cardiac MR and ultrasound images. IEEE Transactions on Medical Imaging. 2002; 21(9):1167–1178. [PubMed: 12564884]

Mitechel, M. An Introduction to Genetic Algorithms. MIT Press; 1998.

Montagnat, J.; Delingette, H. Volumetric Medical Images Segmentation Using Shape Constrained Deformable Models. Vol. 1205. Springer; Berlin/Heidelberg: 1997. p. 13-22.

MR imaging and MR spectroscopic imaging of prostate cancer prior to radical prostatectomy: a prospective multi-institutional clinicopathological study. <http://www.acrin.org/Portals/0/Protocols/6659/A6659partial_summary.pdf>

Nathan, MS.; Seenivasagam, K.; Mei, Q.; Wickham, JEA.; Miller, RA. Transrectal ultrasonography: why are estimates of prostate volume and dimension so inaccurate?. Vol. 77. Blackwell Science Ltd.; 1996. p. 401-407.

Pathak SD, Chalana V, Haynor DR, Kim Y. Edge-guided boundary delineation in prostate ultrasound images. IEEE Transactions on Medical Imaging. 2000; 19(12):1211–1219. [PubMed: 11212369]

Seghers D, Loeckx D, Maes F, Vandermeulen D, Suetens P. Minimal shape and intensity cost path segmentation. IEEE Transactions on Medical Imaging. 2007; 26(8):1115–1129. [PubMed: 17695131]

Smyth PP, Taylor CJ, Adams JE. Automatic measurement of vertebral shape using active shape models. Image and Vision Computing. 1997; 15(8):575–581.

Testa C, Schiavina R, Lodi R, Salizzoni E, Corti B, Farsad M, Kurhanewicz J, Manferrari F, Brunocilla E, Tonon C, Monetti N, Castellucci P, Fanti S, Coe M, Grigioni WF, Martorana G, Canini R, Barbiroli B. Prostate cancer: sextant localization with MR imaging, MR spectroscopy, and 11c-choline PET/CT claudia testa. Radiology. 2007; 244:797–806. [PubMed: 17652190]

Tiwari P, Madabhushi A, Rosen M. A hierarchical unsupervised spectral clustering scheme for detection of prostate cancer from magnetic resonance spectroscopy (MRS). MICCAI. Lecture Notes in Computer Science. 2007:278–286.

Tiwari P, Rosen M, Madabhushi A. Consensus-locally linear embedding (CLLE): application to prostate cancer detection on magnetic resonance spectroscopy. MICCAI. Lecture Notes in Computer Science. 2008; 2:330–338.

Tiwari P, Rosen M, Madabhushi A. A hierarchical spectral clustering and non-linear dimensionality reduction scheme for detection of prostate cancer from magnetic resonance spectroscopy. Medical Physics. 2009; 36(9):3927–3939. [PubMed: 19810465]

Toth R, Chappelow J, Rosen M, Pungavkar S, Kalyanpur A, Madabhushi A. Multi-attribute, non-initializing, texture reconstruction based ASM (MANTRA). MICCAI. Lecture Notes in Computer Science. 2008; 1:653–661.

Toth R, Doyle S, Pungavkar S, Kalyanpur A, Madabhushi A. Weritas: Weighted ensemble of regional image textures for asm segmentation. SPIE Medical Imaging. 2009; 7260

van Ginneken B, Frangi AF, Staal JJ, Romeny B, Viergever MA. Active shape model segmentation with optimal features. IEEE Transactions on Medical Imaging. 2002; 21(8):924–933. [PubMed: 12472265]

Vilanova JC, Barcelo J. Prostate cancer detection: magnetic resonance (MR) spectroscopic imaging. Abdominal Imaging. 2007:253–262. [PubMed: 17476554]

Wang W, Shan S, Gao W, Cao B, Yin B. An improved active shape model for face alignment. Multimodal Interfaces. 2002:523–528.

Warfield, SK.; Zou, KH.; Wells, WM. Validation of Image Segmentation and Expert Quality with an Expectation–Maximization Algorithm. Vol. 2488. Springer; Berlin Heidelberg: 2002. p. 298-306.

Warfield SK, Zou KH, Wells WM. Simultaneous truth and performance level estimation (staple): an algorithm for the validation of image segmentation. IEEE Transactions on Medical Imaging. 2004; 23(7):903–921. [PubMed: 15250643]

Zaider M, Zelefsk MJ, Lee EK, Zakian KL, Amols HI, Dyke J, Cohen G, Hu Y, Endi AK, Chui C, Koutcher JA. Treatment planning for prostate implants using magnetic-resonance spectroscopy imaging. International Journal of Radiation Oncology and Biological Physics. 2000; 47(2):1085–1096.

Zhou J, Kim S, Jabbour S, Goyal S, Haffty B, Chen T, Levinson L, Metaxas D, Yue NJ. A 3D global-to-local deformable mesh model based registration and anatomy-constrained segmentation method for image guided prostate radiotherapy. Medical Physics. 2010; 37(3):1298–1308. [PubMed: 20384267]

Zhu Y, Zwiggelaar R, Williams S. Prostate segmentation: a comparative study. Medical Image Understanding and Analysis. 2003:129–132.

Zhu, Yanong; Fisher, Mark; Zwiggelaar, Reyer. Improving asm search using mixture models for grey-level profiles.. In: Marques, Jorge S.; de la Blanca, Nicols Prez; Pina, Pedro, editors. Pattern Recognition and Image Analysis, Lecture Notes in Computer Science. Vol. 3522. Springer; Berlin/Heidelberg: 2005. p. 292-299.

Zwiggelaar R, Zhu Y, Williams S. Pattern Recognition and Image Analysis. Semi-automatic Segmentation of the Prostate. 2003:1108–1116.
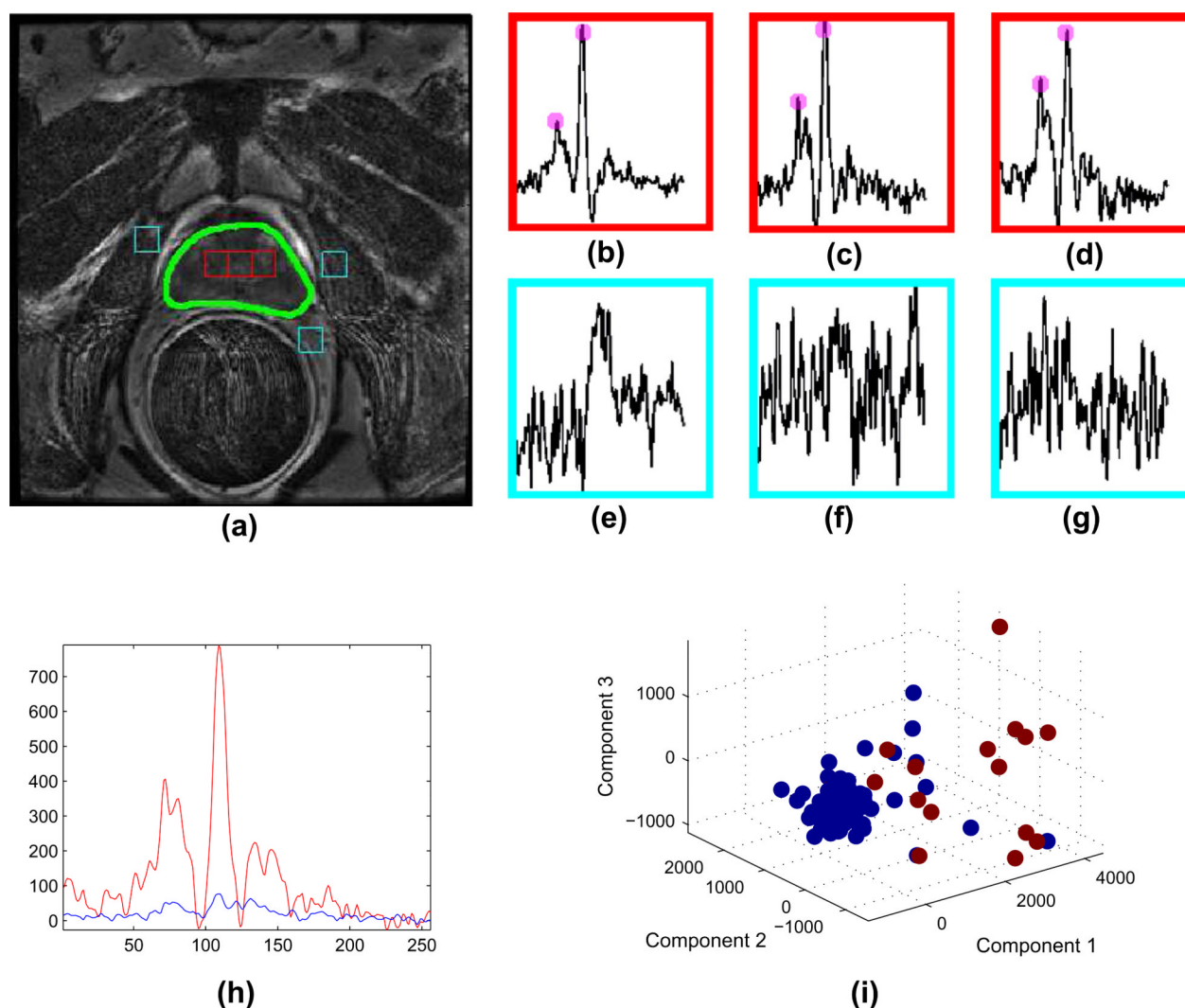
Fig. 1.
(a) 2D section of T2-weighted MR image with the prostate boundary in green. Metavoxels within the prostate are shown in red, and metavoxels outside the prostate are shown in blue. The top of the choline and creatine region is indicated by the left-most purple circle in each of (b)–(d), and the top of the citrate peak is denoted by the right-most purple circle in each of (b)–(d). (h) The mean MRS spectra from the prostate spectra (red) and the extra-prostatic spectra (blue) are shown. (i) Each datapoint represents an MRS spectra (prostate in red, extra-prostatic in blue), in which principal component analysis was used to reduce the 256-dimensional spectra to 3-dimensional spectra for visualization purposes.
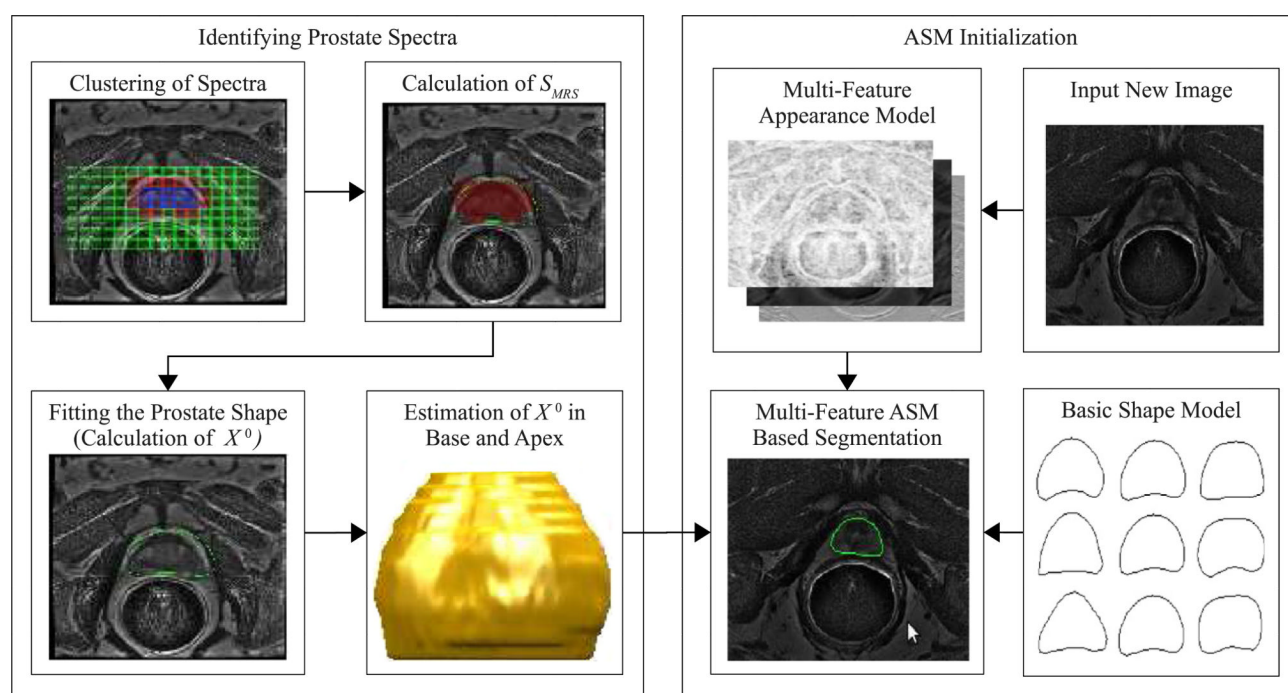
Fig. 2.
Pathways and modules involving in the MRS-based ASM initialization scheme for prostate segmentation on multi-protocol *in vivo* MRI.
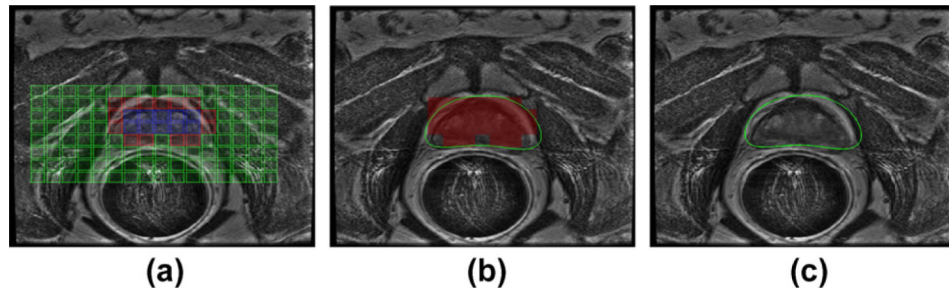
Fig. 3.
(a) MRS metavoxels $\widehat{C}$ (shown as colored boxes) overlaid onto the T2-w image $\mathscr{C}$ where each color represents a different class resulting from the replicated *k*-means clustering scheme. The voxels associated with the informative metavoxels (S_{MRS}) are shown as a red overlay in (b), with the resulting shape initialization $\left(\mathbf{X}^0_{MRS}\right)$ shown as a green line in (b) and (c).
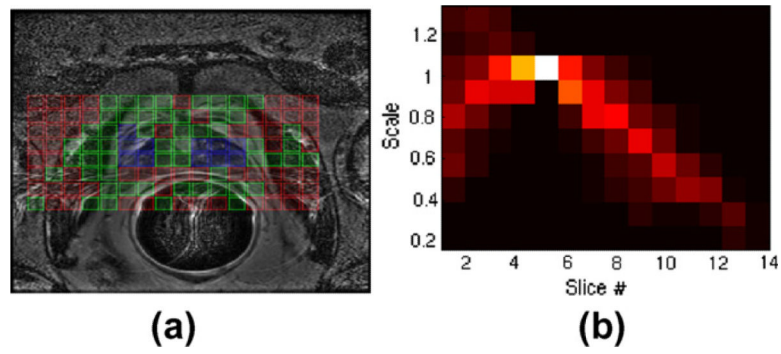
Fig. 4.
(a) Example of a clustering result in the base of the prostate, in which the three colors represent V_a, $a \in \{1, 2, 3\}$. The results demonstrate the degradation of quality of MR spectra in the prostate near the base, a phenomenon which also occurs near the apex. (b) A 2D histogram of the relative size of the prostate as a function of the slice index from base to apex reveals that the prostate is largest in the center and tapers off towards the extrema.
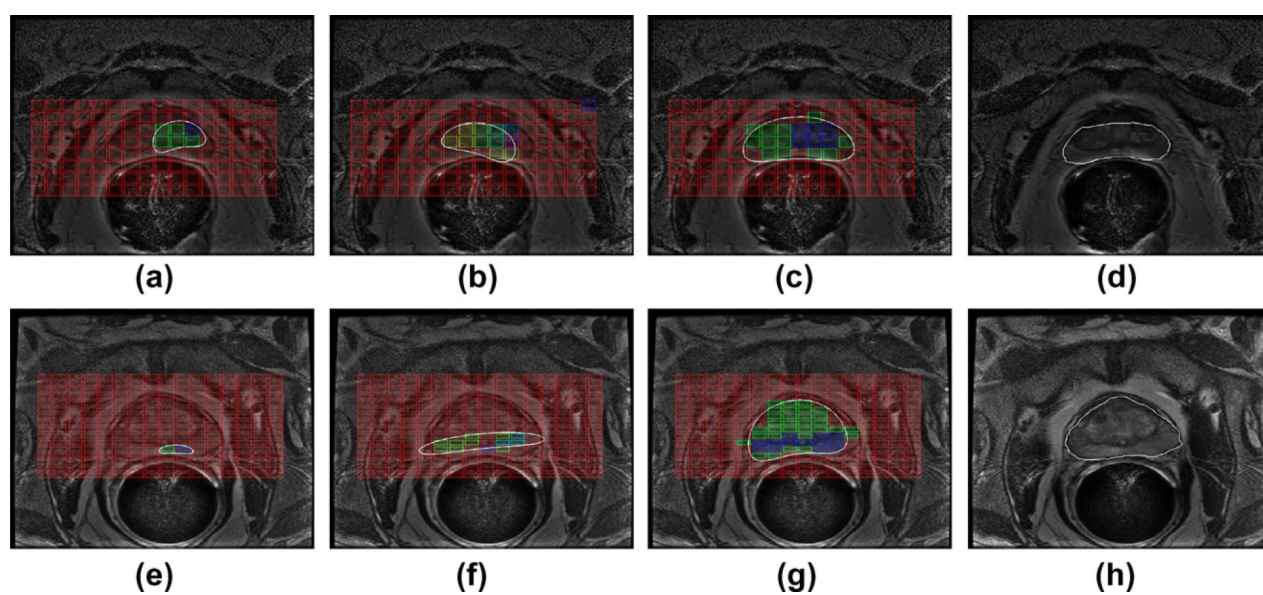
Fig. 5.
Shown above are the qualitative results from $\mathscr{E}_1 - \mathscr{E}_3$ in columns 1, 2, and 3 respectively for two different studies. The color of each metavoxel reflects its class assignment, and the white shape represents $\mathbf{X}^0$. For reference, column 4 shows the ground truth $\mathbf{X}_E$ in white.
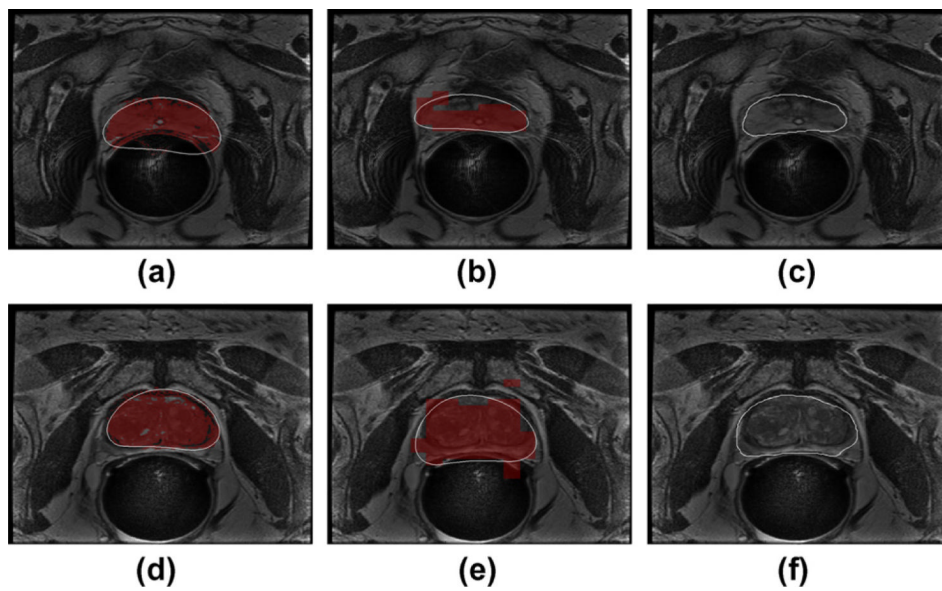
Fig. 6.
S_Δ is shown in red for two different studies (1 study per row), for $\Delta = Cos$ in the first column ((a) and (d)), and $\Delta = MRS$ in the second column ((b) and (e)). The initialization $\mathbf{X}_\Delta^0$ is shown in white, and the ground truth segmentation $\mathbf{X}_E$ is shown in column 3 ((c) and (f)) for reference.
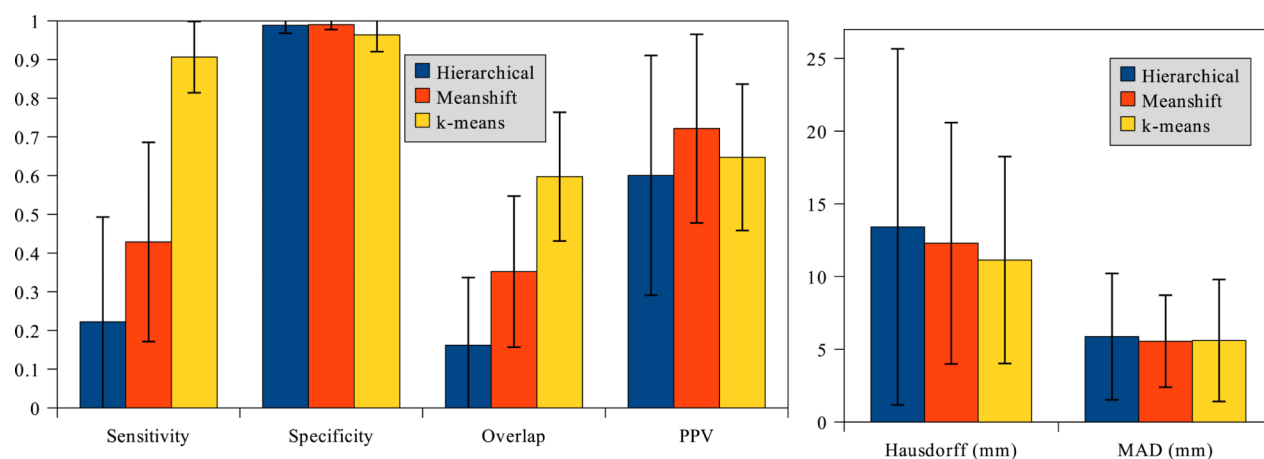
Fig. 7.
Quantitative results for $\mathscr{E}_1 - \mathscr{E}_3$ are shown for the six performance measures over 32 midgland slices, in which the blue bar represents $\mathscr{E}_1$, the red represents $\mathscr{E}_2$, and the yellow represents $\mathscr{E}_3$. The standard deviations over 32 studies are shown with black bars.

(a)

(b)
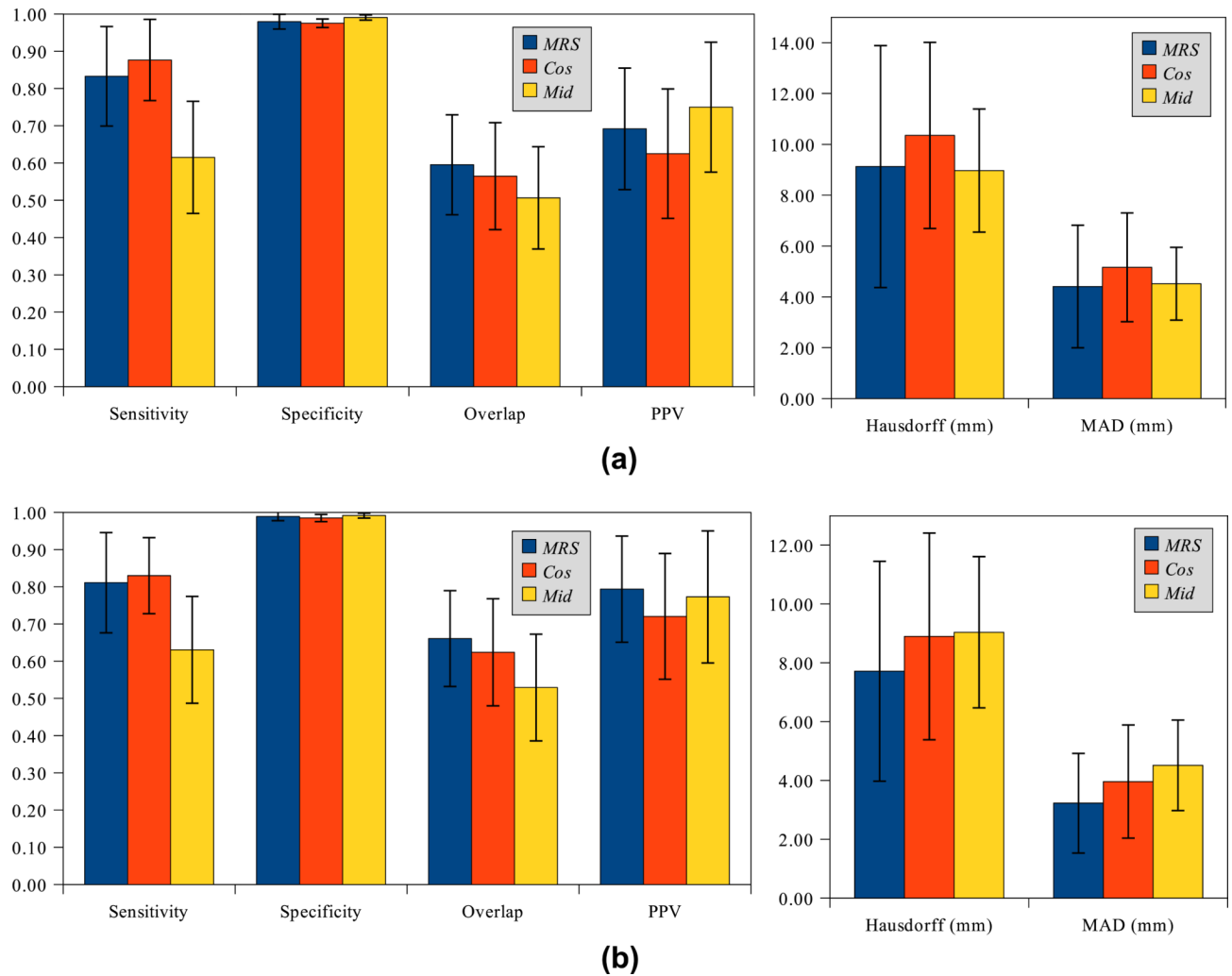
Fig. 8.

(a) Results from the initialization schemes comparing $\mathbf{X}_\Delta^0$ to $\mathbf{X}_E^0$ for each slice, in which $\mathscr{E}_4$ is shown in blue, $\mathscr{E}_7$ is shown in red, and $\mathscr{E}_{10}$ is shown in yellow. The statistical significance results are shown in Table 5. (b) Results from the ASM's comparing $\mathbf{X}_\Delta^{final}$ to $\mathbf{X}_E$ for each slice, in which $\mathscr{E}_5$ is shown in blue, $\mathscr{E}_8$ is shown in red, and $\mathscr{E}_{11}$ is shown in yellow. The statistical significance results are shown in Table 6. Standard deviations over 388 slices are shown as black bars in both (a) and (b).
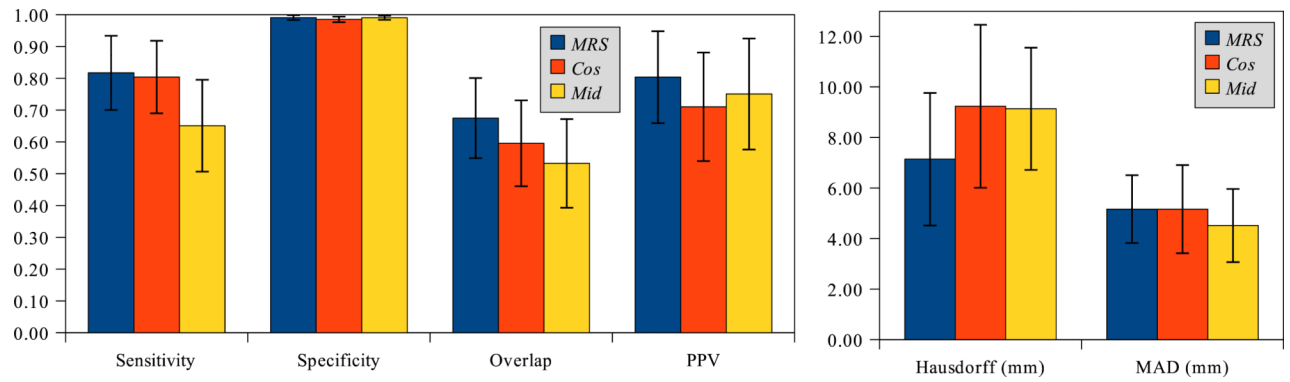
Fig. 9.

Results from the multi-resolution ASM experiments $\mathbf{X}_{\Delta}^{final}$, in which $\mathscr{E}_6$ (the multi-resolution ASM using the MRS initialization) is shown in blue, $\mathscr{E}_9$ (the multi-resolution ASM using the Cosio initialization) is shown in red, and $\mathscr{E}_{12}$ (the multi-resolution ASM using the Midgland initialization) is shown in yellow. The results from the tests of significance, in which each multi-resolution test (shown above) was compared to each non-multi-resolution test (shown in Fig. 8b) are given in Table 7. Standard deviations over all 388 slices are shown as black bars.

Table 1

List of notation and symbols used.

Symbol	Description	Symbol	Description
C	MRI scene	$\hat{C}$	MRS scene
C	Set of spatial coordinates in C	$\hat{C}$	Set of metavoxel coordinates in $\hat{C}$
c	A spatial location in C	$\hat{c}$	A metavoxel in $\hat{C}$
$f(c)$	Intensity value at c	$\hat{F}(\hat{c})$	Spectral content at $\hat{c}$
$S_+ \subset C$	Prostate spatial locations (from experts)	D	Distribution from a sum of Gaussians
$S_\Delta \subset C$	Prostate spatial locations	$\Delta \in \{MRS, Cos\}$	Initialization method employed
$\mathbf{X}$	Set of landmark points ($\mathbf{X} \subset C$)	$\bar{\mathbf{X}}$	Mean training landmark points
$\mathbf{X}_\Delta^0$	Initialized landmarks	$\mathbf{X}_\Delta^{Final}$	Final segmented landmarks

Table 2

Performance measures used.

Measure	Formula
Overlap	$\mid S_{\mathbf{X}_\Delta} \cap S_{\mathbf{X}_E} \mid \, / \, \mid S_{\mathbf{X}_\Delta} \cup S_{\mathbf{X}_E} \mid$
Sensitivity	$\mid S_{\mathbf{X}_\Delta} \cap S_{\mathbf{X}_E} \mid \, / \, \mid S_{\mathbf{X}_E} \mid$
Specificity	$\mid C - S_{\mathbf{X}_\Delta} \cup S_{\mathbf{X}_E} \mid \, / \, \mid C - S_{\mathbf{X}_E} \mid$
Positive predictive value (PPV)	$\mid S_{\mathbf{X}_\Delta} \cap S_{\mathbf{X}_E} \mid \, / \, \mid S_{\mathbf{X}_\Delta} \mid$
Mean absolute distance (MAD)	$\frac{1}{N} \sum_{n=1}^{N} (\| c_n - d_n \|, c_n \in \mathbf{X}_\Delta, d_n \in \mathbf{X}_E)$
Hasudorff distance (HAD)	$\max_n (\| c_n - d_n \|, c_n \in \mathbf{X}_\Delta, d_n \in \mathbf{X}_E)$

Table 3

Experimental set ups for calculation of S_{MRS}.

Experiment	Description
E_1	Hierarchical clustering
E_2	Mean-shift clustering
E_3	Replicated k-means clustering

Table 4

Experimental set ups for the ASM experiments performed.

Experiment	X	Δ	Description
E_4	$\mathbf{X}_\Delta^0$	*MRS*	MRS initialization
E_5	$\mathbf{X}_\Delta^{Final}$		ASM
E_6	$\mathbf{X}_\Delta^{Final}$		Multi-resolution ASM
E_7	$\mathbf{X}_\Delta^0$	*Cos*	Cosio initialization
E_8	$\mathbf{X}_\Delta^{Final}$		ASM
E_9	$\mathbf{X}_\Delta^{Final}$		Multi-resolution ASM
E_{10}	$\mathbf{X}_\Delta^0$	*Mid*	Initialized by placing $\bar{\mathbf{X}}$ in the middle of C
E_{11}	$\mathbf{X}_\Delta^{Final}$		ASM
E_{12}	$\mathbf{X}_\Delta^{Final}$		Multi-resolution ASM

Table 5

Statistical significance results (in terms of p values) between all initialization schemes ($\Delta \in \{MRS, Cos, Midf\}$) are shown below, in which a paired Student's t-test was used to compare two different $\mathbf{X}_\Delta^0$ ($\Delta \in \{MRS, Cos, Midf\}$) results for all six performance measures, over 388 slices. The accompanying data is shown in Fig. 8a.

Comparison	Sensitivity	Specificity	Overlap	PPV	Hausdorff	MAD
E_4, E_7	4.8×10^{-6}	5.8×10^{-4}	1.6×10^{-4}	1.9×10^{-12}	1.3×10^{-4}	3.4×10^{-6}
E_4, E_{10}	1.3×10^{-75}	0	0	2.5×10^{-8}	5.9×10^{-1}	4.7×10^{-1}
E_7, E_{10}	6.9×10^{-114}	3.8×10^{-96}	8.4×10^{-14}	1.7×10^{-55}	7.5×10^{-10}	1.7×10^{-8}

Table 6

Statistical significance results (in terms of p values) between all non-multi-resolution ASM schemes below, in which a paired Student's t-test was used to compare two different $\mathbf{X}_\Delta^{final}$ results for all six performance measures, over 388 slices. The accompanying data is shown in Fig. 8b.

Comparison	Sensitivity	Specificity	Overlap	PPV	Hausdorff	MAD
E_5, E_8	2.2×10^{-2}	8.8×10^{-8}	9.0×10^{-6}	7.8×10^{-16}	2.1×10^{-5}	4.5×10^{-8}
E_5, E_{11}	4.6×10^{-63}	1.2×10^{-4}	0	1.8×10^{-2}	1.6×10^{-8}	0
E_8, E_{11}	1.3×10^{-90}	0	0	3.3×10^{-15}	4.6×10^{-1}	4.3×10^{-4}

Table 7

Statistical significance results (in terms of p values) comparing each $\mathbf{X}_{\Delta}^{final}$ result to the corresponding multi-resolution $\mathbf{X}_{\Delta}^{final}$ segmentation result for all six performance measures over 388 slices. The non-multi-resolution experiments ($\mathscr{E}_5$, $\mathscr{E}_8$, $\mathscr{E}_{11}$) are shown in Fig. 8b and the accompanying multi-resolution experiments ($\mathscr{E}_6$, $\mathscr{E}_9$, $\mathscr{E}_{12}$) are shown in Fig. 9.

Comparison	Sensitivity	Specificity	Overlap	PPV	Hausdorff	MAD
E_5, E_6	2.3×10^{-1}	9.0×10^{-7}	2.3×10^{-3}	2.2×10^{-2}	7.4×10^{-6}	3.5×10^{-4}
E_8, E_9	1.5×10^{-12}	8.7×10^{-1}	0	1.8×10^{-3}	8.3×10^{-4}	5.8×10^{-9}
E_{11}, E_{12}	1.0×10^{-6}	7.6×10^{-13}	3.3×10^{-1}	1.2×10^{-10}	1.9×10^{-1}	4.1×10^{-1}

Table 8

The correlation (R^2 value) between $\mathbf{X}_\Delta^{final}$ and $\mathbf{X}_\Delta^0$ is shown for each performance measure to determine how much of an effect the initialization had on the final ASM segmentation result.

Performance measure	ASM			Multi-resolution		
	E_5	E_8	E_{11}	E_6	E_9	E_{12}
Sensitivity	.81	.71	.80	.65	.80	.84
Specificity	.91	.78	.84	.71	.84	.87
Overlap	.76	.89	.87	.59	.91	.90
PPV	.84	.90	.91	.70	.94	.94
Hausdorff	.88	.86	.82	.68	.85	.84
MAD	.86	.88	.86	.63	.91	.89

Table 9

Efficiency table noting the mean time, in seconds for a single image. For MRS, the time noted is the total time calculating S_{MRS} for a single midgland slice, using k-means clustering replicated 25 times. For Cosio, the time is the calculation of S_{Cos} for a single midgland slice, given that the distributions have already been calculated. The computer system had a 2.8 GHz processor and 32 GB of RAM, running MATLAB 2009b with the Ubuntu Linux operating system.

	MRS	Cosio	ASM
Mean time (s)	1.3	0.08	0.14